Environmental Science Nano

ROYAL SOCIETY OF CHEMISTRY

PAPER

View Article Online
View Journal | View Issue

Cite this: *Environ. Sci.: Nano*, 2026, **13**, 1435

^{14}C-labelled nanoplastics reveal size-dependent bioaccumulation in juvenile rainbow trout (*Oncorhynchus mykiss*)

Maya Al-Sid-Cheikh, †*[a] Joyce W. L. Ang, [b] Gareth T. W. Law, [b] Ana I. Catarino, ‡[c] Theodore B. Henry, [c] Steve J. Rowland, [d] Marc-Andre Cormier §[e] and Richard C. Thompson [a]

Concerns have been raised about the occurrence of nanoplastics (NP) in the environment. Herein we investigated size-dependent uptake, biodistribution, and egestion of 20 and 250 nm [^{14}C]nanopolystyrene in juvenile rainbow trout (*Oncorhynchus mykiss*) at environmentally relevant concentrations: a single-day "high-dose" (250 ng $g_{w.w.}^{-1}$ (~ppb) fed once) and a 5 day "low-dose" (8 ng $g_{w.w.}^{-1}$). Following single-day 'high' dose exposure, 20 nm particles – but not 250 nm – were detected in internal tissues, indicating translocation across gut endothelia. Rapid depuration returned NP concentrations to control levels within 10 days, with no evidence of accumulation in organs. The presence of 20 nm NPs in circulation suggests temporary vascular transport without parenchymal retention. Translocation of 20 nm NPs across the gut endothelia and association with blood cells should be investigated to determine the cell types involved and the outcome of these associations. These results indicate that uptake-depuration kinetics for [^{14}C] nanopolystyrene in rainbow trout differ from those of other chemical substances (*e.g.*, metals, persistent organic pollutants) and likely have different implications on organism health. The results of this study and the methods developed provide a means of studying and comparing the fate of NPs in organisms such as bivalves and fish.

Received 25th October 2025,
Accepted 13th January 2026

DOI: 10.1039/d5en00985e

rsc.li/es-nano

Environmental significance

Detection of nanoplastics at environmentally realistic concentrations remains analytically challenging. By combining intrinsic ^{14}C-labelling with quantitative whole-body autoradiography (QWBA), we resolve size-dependent uptake, transient systemic distribution, and rapid depuration of 20 nm and 250 nm polystyrene nanoplastics in juvenile trout under environmentally relevant low-dose dietary exposure. These data clarify how particle size and exposure design govern biodistribution at relevant concentrations and provide benchmarks to inform ecological risk assessment.

Introduction

Nanoplastics (NPs; defined as plastic particles smaller than 1 μm (ref. 1–4) are a growing environmental concern due to their ability to cross biological barriers,[5] raising concerns about potential bioaccumulation and transfer through food webs, which could make them one of the most hazardous forms of plastic litter.[6] Global plastic production continues to rise, with 9–14 million tonnes of plastic litter entering the environment annually, potentially increasing to 23–37 million tonnes by 2040.[7–10] Despite international efforts, including the ongoing negotiations of the United Nations Plastic Pollution Treaty (INC-4, 2024), understanding of NP behaviour in organisms and ecosystems remains limited, largely due to analytical challenges associated with detecting small particles at environmentally relevant concentrations. Predicted environmental concentrations of NPs—for example, 1 pg L^{-1} to 15 μg L^{-1} for ~50 nm particles and below 0.5 μg

[a] *School of Biological and Marine Sciences, University of Plymouth, Drake Circus, Plymouth, PL4 8AA, UK. E-mail: malsid@ed.ac.uk*
[b] *Radiochemistry Unit, Department of Chemistry, Faculty of Science, University of Helsinki, A.I. Virtasen Aukio 1, P.O. Box 55, Helsinki, FI-00014, Finland*
[c] *School of Geography, Earth and Environmental Sciences, University of Plymouth, Drake Circus, Plymouth, PL4 8AA, UK*
[d] *Institute of Life and Earth Sciences Heriot-Watt University, John Muir Building, Edinburgh, EH14 4AS, UK*
[e] *Department of Earth Sciences, University of Oxford, South Parks Road, Oxford, OX1 3AN, UK*
† Present address: EaStCHEM School of Chemistry, University of Edinburgh, Joseph Black Building, Edinburgh, EH9 3FJ, United Kingdom.
‡ Present address: Flanders Marine Institute (VLIZ), Research Division, Ocean and Human Health, InnovOcean Campus, Jacobsenstraat 1, 8400 Oostende, Belgium.
§ Present address: School of Geographical & Earth Sciences, University of Glasgow, Main Building, Glasgow, G12 8QQ, United Kingdom.

L^{-1} for 5 μm particles—are orders of magnitude lower than those often used in laboratory studies.[11] Despite these low concentrations, studies have shown that NPs can translocate within organisms.[5]

Laboratory-based experiments complement environmental monitoring by allowing precise control over NP parameters such as size, morphology, concentration, water chemistry, and exposure regimes. Although these experiments may not fully replicate ecological conditions, they allow investigation of NP behaviour and mechanisms of action, particularly under chronic or complex exposure scenarios. However, experimental studies have been criticized for using particle concentrations in single-day high-dose exposures that exceed environmentally realistic levels.[11–13] For example, studies using extrinsic labelling of metal-doped nanopolystyrene (nPS) required excessively high feed concentrations (10 mg Pd as PS–Pd NPs per kg^{-1}, ~2 g NPs per kg) to detect particles in tissues,[14,15] emphasizing the difficulty of measuring NPs at environmentally realistic concentrations. While such high doses provide mechanistic insight, they risk misinterpreting the potential impact of NPs on organisms and ecosystems,[16] underscoring the need for studies at environmentally relevant concentrations. Moreover, differences in polymer type and particle morphology may also influence NP behaviour, as polyethylene and polypropylene, or fibres *versus* spheres, display distinct aggregation and uptake dynamics that remain underexplored in toxicokinetic studies.

Intrinsic radiolabelling of nPS with ^{14}C enables sensitive quantification of NPs at predicted concentrations (<10 μg L^{-1}) and small particle sizes (down to 20 nm,[5,17]), addressing previous analytical limitations. By incorporating ^{14}C into the polymer backbone, quantitative whole-body autoradiography (QWBA) enables spatially resolved tracking of NP accumulation in tissues, eliminating cross-contamination risks inherent to dissection-based methods.[18–20] This method significantly enhances sensitivity and spatial resolution, enabling detection and quantification of NPs in organ substructures and biological fluids, providing a detailed, contamination-free profile of NP distribution.[19,20] QWBA has been validated over 20 years as the 'gold standard[21] for producing reliable and precise tissue concentration data, offering accuracy and reproducibility.[20] While liquid scintillation counting (LSC) remains a complementary and widely used method for quantifying radiotracers, its reliance on bulk dissection makes it more prone to contamination artefacts, which QWBA can overcome. Together, these approaches allow comparison of NP behaviour based on size: smaller particles (<100 nm) may penetrate biological barriers more readily, while larger particles (>100 nm) may accumulate differently or be cleared *via* distinct pathways.[5,22–24] Such spatially resolved toxicokinetic data are essential to understand NP behaviour, uptake, depuration, and potential toxicity in vertebrates.

We selected nPS as a model system due to its widespread production, accounting for approximately 7% of global polymer output (US Department of Energy, 2024), and its prevalence in environmental samples.[25] Its well-characterized chemical structure and predictable behaviour make it an ideal standard material. Incorporation of ^{14}C enables QWBA of [^{14}C]nPS in biological specimens. We investigate the toxicokinetics (*i.e.* uptake and depuration) of small (20 nm, nPS_{20}) and large (250 nm, nPS_{250}) nPS in rainbow trout (*Oncorhynchus mykiss*), under two exposure scenarios: a single-day high-dose exposure (250 ng $g_{w.w.}^{-1}$) and a short-term, environmentally relevant exposure (8 ng $g_{w.w.}^{-1}$ for 5 days). The smaller size (20 nm) was selected to represent particles capable of crossing biological barriers and entering systemic circulation, as reported for nanoparticles below 100 nm.[26–30] The inclusion of 250 nm particles reflects the upper nanoscale range, relevant to environmental NPs and regulatory definitions, and enables assessment of size thresholds for biological barrier penetration. These sizes were chosen not only for comparison but also to evaluate potential limitations in crossing biological barriers such as gut epithelia and lymphoid tissues, which are known to restrict particles above ~200 nm.[23,24,31] This approach enables assessment of size-dependent uptake mechanisms, clearance dynamics, and tissue distribution under controlled conditions in the vertebrate model—critical for accurate environmental risk assessment. By integrating intrinsic radiolabelling with high-resolution autoradiography, this study provides the first spatially resolved quantification of NP biodistribution and clearance in fish exposed to environmentally relevant concentrations.

Materials and methods

Radiosynthesis of [^{14}C]-polystyrene nanoparticles

Radiolabelled polystyrene nanoparticles ([^{14}C]nPS) originated from the same batch previously described and characterized in Al-Sid-Cheikh *et al.*[17] Full synthesis details and physicochemical characterization, including particle size distribution, morphology, and radiolabel incorporation, are provided in that publication and summarised in Text S1. A [^{14}C]-styrene tracer (specific activity 2.22 GBq $mmol^{-1}$, ARC Inc.) was incorporated into the polymerisation mixture, and the unreacted monomer was removed by repeated ultrafiltration (30 kDa cut-off). Two size fractions were produced—nominal diameters of 20 nm ([^{14}C]nPS_{20}) and 250 nm ([^{14}C]nPS_{250})—representing the nanoscale and submicrometre size ranges relevant to environmental exposure.

Hydrodynamic size and surface charge were determined by dynamic light scattering (DLS) and surface charge (zeta potential) was measured in ultrapure water (18.2 MΩ cm), pH 6 in a sodium chloride solution (5 mM), 25 °C. Polydispersity index (PDI) values were 0.07 for [^{14}C]nPS_{20} and 0.08 for [^{14}C]nPS_{250}, consistent with narrow size distributions. Particle size and morphology were confirmed by transmission electron microscopy (TEM). Representative mean diameters were 25 ± 13 nm and 248 ± 21 nm with zeta potentials of −129 ± 10 mV

(20 nm) and −84 ± 12 mV (250 nm), respectively. FTIR and Raman spectra were consistent with the polystyrene backbone (Fig. S1). The detailed synthesis conditions, purification steps, and full physicochemical characterisation are provided in Text S1 and Al-Sid-Cheikh *et al.* (2020).

Ethical approval and animal husbandry

Ethical approval. All animal experimental procedures were approved by the Radioprotection and Animal Welfare Committee at Heriot-Watt University (Scotland, United Kingdom). Experiments were conducted in accordance with UK Home Office regulations under Project Licence PL Number P70BAC026 (Principal Investigator: TB Henry). Juvenile rainbow trout (*Oncorhynchus mykiss*) were handled following the approved protocols, and euthanasia was performed in accordance with Schedule 1 of the UK Animals (Scientific Procedures) Act 1986.

Fish husbandry and stocking. Juvenile rainbow trout (*O. mykiss*) were acclimated for 14 days prior to exposure in 1000 L recirculating tanks under a 12 : 12 h light : dark cycle. Fish were fed commercial pellets (Nutrafin Basix A-7176) at 2% body weight per day. Exposure tanks were stocked at ∼7–11 g L^{-1} (28–32 fish of ∼17 ± 2 $g_{w.w.}$ per 60 L tank), a loading that, under continuous flow and oxygenation, maintains stable dissolved oxygen and nitrogenous wastes while supporting normal feeding behaviour. The exposure design followed UK Home Office husbandry standards.

[^{14}C]-labelled feed preparation

Pelletisation method. Commercial dry pellets (Nutrafin Basix A-7176) were hydrated with ultrapure water at a water : food ratio ≈ 0.5 : 1 (50 g water per 100 g dry feed) to form a homogeneous paste. The paste was spread on a coated, non-stick bench to a thickness of a few millimetres and passed through a metallic mesh to produce uniform pellets. Pellets were dried at 50 °C overnight and stored at room temperature in the dark until use.

Dose formulation. Ultrapure water containing [^{14}C]nPS_{20} or [^{14}C]nPS_{250} was mixed into the feed paste to achieve target activities of:

– Single-day high-dose: 250 ± 21.2 ng ^{14}C per $g_{w.w.}$ (14.8 kBq $g_{w.w.}^{-1}$)

– Low-dose: 8 ± 0.8 ng ^{14}C per $g_{w.w.}$ (4.1 kBq $g_{w.w.}^{-1}$)

For a batch of 100 g dry feed + 50 g water (wet weight 150 g), the total [^{14}C]nPS required was 37.5 μg (high-dose) and 1.2 μg (low-dose). Batch homogeneity was assessed by LSC (see Solid-sample method) on subsamples taken across the batches.

Leaching control. Leaching of [^{14}C]nPS from the feed was evaluated using triplicate pre- and post-feeding tank water samples for both exposure scenarios. Daily water samples were additionally collected to track excretion into the water column. All the samples were analysed by LSC (See liquid-sample method), and activities were consistently below the minimum detectable activity (MDA; 0.07 Bq g^{-1}), across all sampling points, confirming negligible feed-derived leaching.

Exposure design

System and water quality. Experiments were conducted in single-pass, flow-through 60 L tanks supplied continuously with dechlorinated Edinburgh municipal water *via* serial activated-carbon filtration (free chlorine below detection), followed by zeolite ion-exchange for ammonium control. Per-tank flow was set to 12.5 L h^{-1}, equivalent to 5 tank volumes per day and a hydraulic residence time of ∼4.8 h, consistent with flow-through practice exemplified in the OECD Test Guideline 203 (≥5 tank volumes per 24 h). Water quality was maintained within rainbow-trout husbandry ranges (8–10 °C; conductivity ≈ 250 μS cm^{-1}; [Ca^{2+}] ≈ 1 mM; pH 7.5–8.0), with dissolved oxygen at saturation. Temperature, pH, conductivity, dissolved oxygen were logged daily.

Feeding protocol and dosing. Fish were fasted for 24 h prior to exposure. Spiked pellets (prepared as described in *Feed preparation*) were delivered as group feeding at the tank level, with rations calculated from the mean wet biomass per tank to achieve the intended dose (ng $g_{w.w.}^{-1}$). To ensure complete consumption and avoid loss of pellets to the outflow, incoming water was briefly paused (static mode) for a few minutes during feeding and resumed immediately once all pellets had been consumed.

– Single-day high-dose exposure: one meal formulated to deliver 250 ng $g_{w.w.}^{-1}$.

– Five day low-dose exposure: one meal per day for 5 consecutive days at 8 ng $g_{w.w.}^{-1}$ d^{-1}.

After the exposure period, fish were returned to the standard commercial diet (unspiked Nutrafin Basix A-7176) at the acclimation ration (∼2% body mass per d) for the duration of depuration.

Intake verification. Feeding was visually monitored throughout: all pellets were consumed (*i.e.* 100% ingestion of the [^{14}C]nPS) within minutes, and no dominance or unequal intake was observed.

Replicates and controls. Two replicate tanks per treatment were used. At each timepoint, fish were euthanised by overdose of MS-222 (tricaine methanesulfonate), rinsed, and prepared for either toxicokinetic (TK, *i.e.* total ^{14}C LSC) or tissue distribution (*i.e.* QWBA). Two fish per replicate tank (n = 4 per timepoint) were sampled for LSC and QWBA. A total of 324 fish were used across all treatments (Table S1). Controls comprised particle-free feed and unlabelled nPS (size-matched) to verify background ^{14}C and rule out artefacts from the polymer matrix. Control fish were sampled at the same timepoints as exposed fish (see below).

Sampling schedule and allocation. – Single-day high-dose exposure followed by 13 days of depuration with sampling at 0.2, 0.8, 1, 2, 4, 7, 8, 10, and 13 days.

– Five day low-dose exposure followed by 10 days of depuration with sampling at 1, 3, 6, 7, 9, 12, and 15 days (where day 1 corresponds to the first exposure day).

T_0 corresponds to the start of the exposure. Control fish (particle-free feed and unlabelled nPS) were sampled at the same timepoints.

Total radiocarbon (C) quantification

Solid-sample method for food, tissues and faeces. All solid matrices (dietary pellets, whole-body tissues and faeces) were prepared using a unified solid-sample protocol. All solid samples were weighed on analytical balances. Briefly, weighed solids were digested in *Solvable*™ (PerkinElmer, USA), an aqueous quaternary ammonium hydroxide solubiliser, at a ratio of 1 mL per 100 mg of sample in 20 mL glass scintillation vials. Vials were incubated at 55 °C for 2 h to achieve complete solubilisation. To eliminate residual colour and minimise quenching, 30% H_2O_2 was added at 100–200 μL per mL of Solvable, followed by an additional 45 min incubation at 55 °C until solutions were clear. After cooling to room temperature, digests were combined with *Ultima Gold*™ scintillation cocktail (PerkinElmer) at a ratio of 2.5 mL digest to 10 mL cocktail, capped, mixed gently, and equilibrated for 24 h in the dark prior to counting on a Hidex 300SL. Each analytical batch included procedural blanks and ^{14}C standards; instrument performance was verified daily.

Food pellets (dietary feed). Individual pellets (typically 50–200 mg post-drying) were digested and counted as above. To verify pellet-to-pellet homogeneity, 5–10 pellets per feed batch were analysed and the relative standard deviation (RSD) reported. The five-day low-dose feed (nominal 8 ng g^{-1} d^{-1}) showed RSD = 9.8%, corresponding to 8.00 ± 0.78 ng g^{-1} and per feeding day. The single-day high-dose feed (nominal 250 ng g^{-1}; batch activity 14.8 kBq) showed RSD = 8.5%, corresponding to 250.0 ± 21.25 ng g^{-1}. These values (<10% RSD) confirm the homogeneous distribution of [^{14}C]nPS in the prepared feeds.

Whole-body tissues. For toxicokinetic analysis, each fish was processed as a whole-body sample rather than dissected organs to avoid cross-contamination and to pair with QWBA for spatial resolution. Fish were blended to a uniform homogenate, freeze-dried, and ground to a fine powder. From each homogenised fish, 10 aliquots were collected to ensure representative sampling; ≤200 mg aliquots were digested and counted following the protocol above. Tissue concentrations are reported as ng $g_{w.w.}^{-1}$ and/or kBq g^{-1}, with wet-weight values back-calculated from dry-aliquot data using fish-specific moisture factors.

Faeces. Faeces were collected daily prior to feeding (during exposure and depuration), immediately frozen (−20 °C), then freeze-dried, homogenised to a fine powder, and analysed by LSC using the solid-sample protocol (*Solvable*™ digestion, H_2O_2 bleaching; typical aliquots 50–200 mg). Results are reported as ng g^{-1} or kBq g^{-1}.

Liquid-sample method. Tank water was sampled from the mid-water column using pre-rinsed glass pipettes to avoid bottom disturbance and transferred into 20 mL glass scintillation vials. 10 mL of water was combined with 10 mL *Ultima Gold*™ scintillation cocktail (PerkinElmer) to achieve a single-phase mixture suitable for aqueous counting. Vials were capped and inverted gently to avoid aerosol formation prior to counting on a Hidex 300SL. Each batch included procedural blanks prepared from the same dechlorinated municipal water used for husbandry; blank count rates were subtracted from all measurements. Triplicate vials were prepared per sampling point (routine daily samples for TK mass balance, and pre- and post-feeding on exposure days to assess potential leaching from feed).

Liquid scintillation counting (LSC, Hidex 300 SL)

Instrument. Activities of ^{14}C-labelled samples were measured on a Hidex 300 SL liquid scintillation counter operated in triple-coincidence (TDCR) mode with three PMTs (120° geometry). TDCR provides absolute activity counting without internal/external standards and mitigates chemiluminescence artefacts; an external standard option is available but was not required.

Counting windows and spectra. Regions of interest (ROI) for ^{14}C β-emission were defined in MikroWin using the instrument's beta spectra and QPE/QPI indicators; ROI placement followed Hidex guidance for window selection and was verified against unquenched and matrix-matched standards.

Quench correction. Quench and counting efficiency were determined automatically by TDCR, with efficiency calculated from the ratio of triple to double coincidences. Where required, a TDCR quench curve was generated from ^{14}C standards and applied by MikroWin (cubic-spline fit). Channel-ratio and external-standard procedures are supported but were not used.

Detection and quantification limits. For food, tissues and faeces measured by LSC, the limit of detection (LOD) and limit of quantification (LOQ) for ^{14}C were 3.14×10^{-3} ng $g_{w.w.}^{-1}$ and 8.62×10^{-3} ng $g_{w.w.}^{-1}$, respectively. The minimum detectable activity (MDA) used in leaching checks of tank water was 0.07 Bq g^{-1}. Comprehensive LOD/LOQ values for all matrices and methods (including QWBA) are provided in Table S2.

Quality assurance and quality control (QA/QC). Each LSC batch included procedural blanks (*Solvable*™/H_2O_2/cocktail without sample) to establish background and the MDA; blank counts were subtracted from all the samples. Instrument performance was verified daily with traceable ^{14}C standards and internal controls, and quench/efficiency were monitored by the instrument's TDCR quench curve in MikroWin. Samples were measured in triple-coincidence mode to minimise chemiluminescence effects; 24 h dark equilibration was applied for consistency prior to counting. Recovery checks were performed by spiking known activities of [^{14}C] standards into representative matrices (food, tissue, faeces) and were accepted when within 90–110% of expected values.

Quantitative whole-body autoradiography (QWBA)

Whole-body autoradiography was conducted on fish sampled from both single-day high-dose and five-day low-dose exposure experiments to visualise tissue distribution of [^{14}C] nPS. Fish were embedded in 2.5% carboxymethyl cellulose, flash-frozen in a liquid N_2 bath, and cryosectioned (20 μm) every 0.75 mm. Sections were mounted on tape and exposed for 7 days to phosphor imaging plates, then scanned at 25 μm resolution using a Typhoon FLA 9000. Quantification was performed using AIDA v5.0 SP3 software with calibration against ^{14}C polymer standards.

Autoradiograms were validated using internal (serum-embedded or PMMA-embedded) standards and cross-checked on an alternative digital autoradiography platform (BeaQuant). Comparison of the two systems confirmed linearity of response ($R^2 > 0.99$) and no detectable bias (Full details in Text S2; Fig. S2 and S3). The limit of detection (LOD) and limit of quantification (LOQ) for both analytical techniques are reported in Table S2 of the SI.

Toxicokinetic modelling

Time-resolved tissue concentrations were fitted to first-order one-compartment models using the MOSAIC$_{bioacc}$ web platform.[32–34] Uptake (k_{uf}) and elimination (k_{ee}) rate constants, biological half-lives ($t_{1/2}$), and biomagnification factors (BMF_k, BMF_{ss}) were derived by Bayesian inference. Model performance was evaluated through posterior predictive checks and 95% credibility intervals. Full model specifications and parameter tables are provided in Text S3 and Fig. S5 and S6.

Statistical analyses

All data were processed in R (v4.3.1). Two-way ANOVA followed by Tukey's *post hoc* tests was used to test the effects

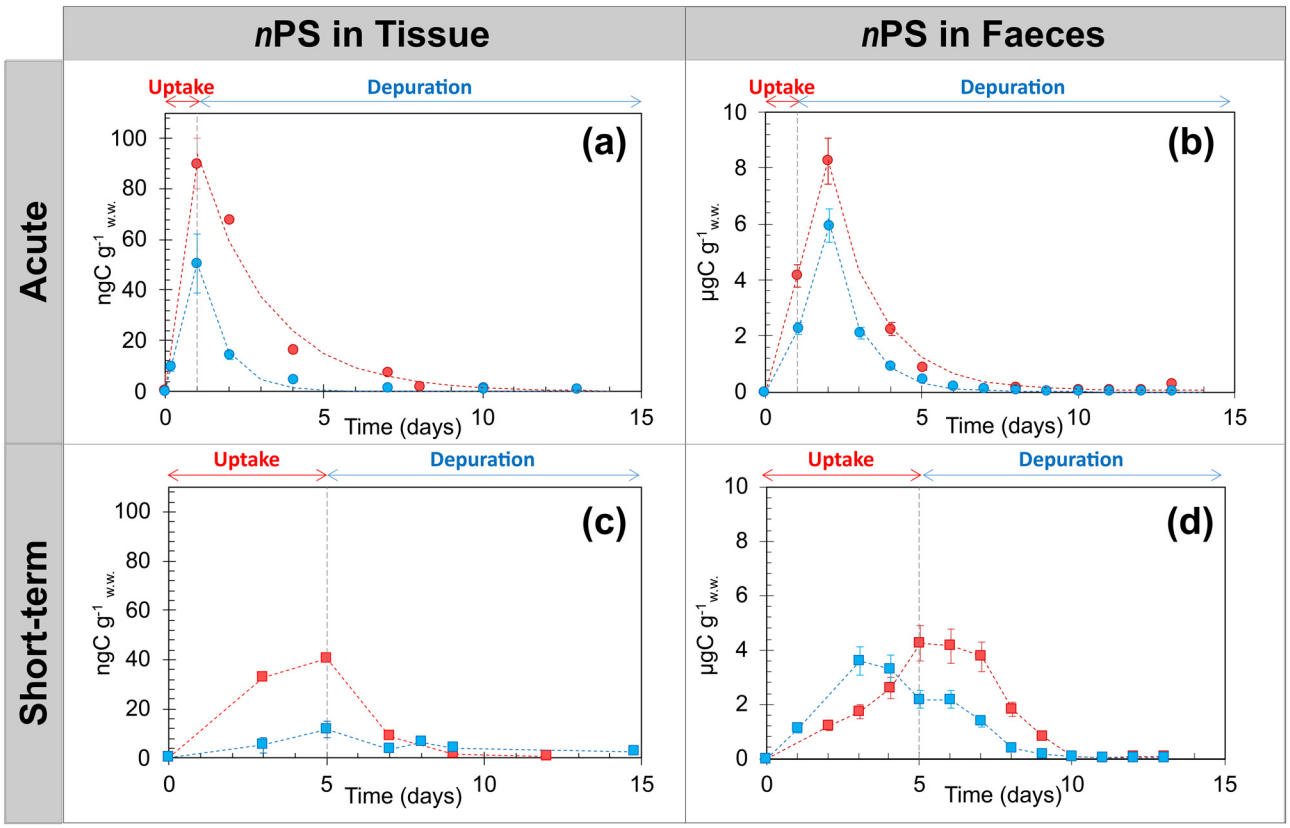

Fig. 1 Quantification of ^{14}C NP in (a) *O. mykiss* tissues and (b) faeces over time. Subfigure (a) displays the ^{14}C concentrations in tissues following single-day high-dose exposure to 250 ng $g_{w.w.}^{-1}$ of 20 nm (red circles) and 250 nm (blue circles) ^{14}C labelled nPS at 250 ng $g_{w.w.}^{-1}$ in food, while (b) shows the corresponding ^{14}C concentrations in faeces during the same exposure. Subfigure (c) presents the concentrations in tissues after lower dose exposure over 5 days to 8 ng $g_{w.w.}^{-1}$ of 20 nm (red squares) and 250 nm (blue squares) ^{14}C labelled nPS, while (d) shows the corresponding ^{14}C concentrations in faeces following the same exposure. The data points show the concentrations of polystyrene nanoparticles (ng g^{-1}) of tissue wet weight or of (μg g^{-1}) faeces dry weight as mean ± S.D., where n = 6 or 7 per data point. These data can also be expressed as the number of particles per gram of wet weight (SI, Text S2). Blue and red dotted lines are fitting curves except for (c and d). Complete regression analyses show different kinetics, including a larger bioconcentration factor for smaller particles, given in the SI (Fig. S4 and S5, Text S3 and Table S4). The grey vertical dotted line indicates the end of the uptake period and the beginning of the depuration period. Note: feed was consumed within minutes. Uptake is displayed over the first day to capture post-prandial GI transit, absorption and systemic distribution until tissue activity exceeded detection thresholds. Tanks were briefly static during feeding (few minutes); flow-through resumed immediately thereafter. All pre-/post-feeding water samples were below MDA/LOD (0.07 Bq g^{-1}), confirming negligible leaching.

of particle size and dose. Results are presented as mean ± SD, and significance was accepted at $p < 0.05$.

Results

Toxicokinetics (TK): uptake and depuration

Daily ^{14}C measurements were conducted on tissues (Fig. 1a and c) and faeces (Fig. 1b and d) of *O. mykiss* exposed to [^{14}C]nPS$_{20}$ (pink circles) and [^{14}C]nPS$_{250}$ (blue circles) under two exposure scenarios: a single-day high-dose (single feed at 250 ng $g_{w.w.}^{-1}$) and short-term low-dose (5 day feed at 8 ng $g_{w.w.}^{-1}$, Fig. 1). Although all feed was consumed within minutes, uptake is shown over the first day to reflect the time required for gastrointestinal transit and systemic absorption of NPs. The limits of detection (LOD) and quantification (LOQ) for ^{14}C using liquid scintillation counting were 3.14×10^{-3} ng $g_{w.w.}^{-1}$ and 8.62×10^{-3} ng $g_{w.w.}^{-1}$, respectively (Table S2).

The single-day high-dose (250 ng $g_{w.w.}^{-1}$) exposure resulted in the highest tissue concentrations, reaching 90.0 ± 6.8 ng_C $g_{w.w.}^{-1}$ for [^{14}C]nPS$_{20}$ and 51.0 ± 11.9 ng_C $g_{w.w.}^{-1}$. for [^{14}C]nPS$_{250}$ after a single day (Fig. 1a). Tissue concentration of [^{14}C]nPS$_{250}$ was consistently lower than that of [^{14}C]nPS$_{20}$ (~0.3 and 9.1 times lower, p-value < 0.001, t test, $n = 4$). In faeces, peak concentrations occurred after 2 days (8.3 ± 0.9 μg_C $g_{w.w.}^{-1}$ for [^{14}C]nPS$_{20}$; 6.0 ± 0.6 μg_C $g_{w.w.}^{-1}$ for [^{14}C]nPS$_{250}$; Fig. 1b). Both tissues and faeces exhibited exponential depuration, with near-complete elimination within six days.

During the 5 day low-dose exposure, tissue accumulation reached 40.1 ± 3.1 ng_C $g_{w.w.}^{-1}$ ([^{14}C]nPS$_{20}$) and 11.8 ± 1.0 ng_C $g_{w.w.}^{-1}$ ([^{14}C]nPS$_{250}$) after three days (Fig. 1c). The concentration of [^{14}C]nPS$_{20}$ was consistently higher than that of [^{14}C]nPS$_{250}$, by approximatively 0.2- to 6.3-fold (Fig. 1c). The concentrations of [^{14}C]nPS in the tissues decreased rapidly between 3 and 6 days. A notable difference was also observed between [^{14}C]nPS$_{20}$ and [^{14}C]nPS$_{250}$ concentrations in faeces (Fig. 1d). The peak faecal concentration of [^{14}C]nPS$_{250}$ (3.6 ± 0.4 μg_C $g_{w.w.}^{-1}$) occurred after 3 days of exposure, whereas the peak for [^{14}C]nPS$_{20}$ (4.2 ± 0.5 μg_C $g_{w.w.}^{-1}$) was observed after 5 days, coinciding with the end of the exposure period (Fig. 1d). The concentration patterns in faeces during the depuration phase (from day 6 onwards) were similar for both particle sizes, although the larger particles exhibited a faster depuration rate than the smaller ones (Fig. 1d). These differences suggest size-dependent elimination rates or clearance mechanism between the two particle sizes. By day 10, depuration from the tissues was complete for both NP sizes, as confirmed by the low [^{14}C] levels measured in both tissues and faeces.

MOSAIC modelling

MOSAIC$_{bioacc}$ provided posterior distribution for the uptake rate *via* food (k_{uf}, d^{-1}), elimination rate *via* excretion (k_{ee}, d^{-1}), and BMF, reported as kinetic BMF (BMF$_k$) and the steady-state BMF (BMF$_{ss}$, Fig. 2). In toxicokinetics, BMF involves at least two trophic levels: the prey (lower trophic level) and the predator (higher trophic level). BMF is defined as the ratio of contaminant concentration in the predator to that in the prey. In this TK model, the term 'bioaccumulation metrics' is used generically to denote BMF when exposure occurs *via* the food,[33] and does not necessarily refer to a classical prey–predator relationship. In our study, fish were fed homemade pellets distributed uniformly throughout the tanks, which they consumed as their primary food source.

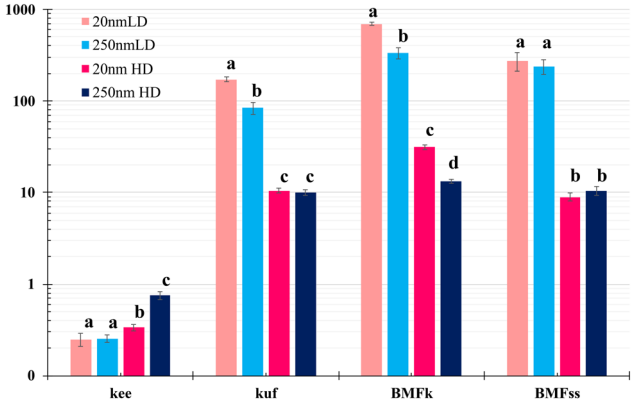

Fig. 2 Mean ± S.D. of bioaccumulation kinetic parameters provided by MOSAIC$_{bioacc}$. Numbers with different letters are significantly different ($p < 0.05$). Light pink: [^{14}C]nPS$_{20}$, short-term low-dose (8 ng $g_{w.w.}^{-1}$ for 5 days); light blue: [^{14}C]nPS$_{250}$, short-term low-dose (8 ng $g_{w.w.}^{-1}$ for 5 days); dark pink: [^{14}C]nPS$_{20}$, single-day high-dose exposure (250 ng $g_{w.w.}^{-1}$ for 1 days); and dark blue: [^{14}C]nPS$_{250}$, single-day high-dose exposure (250 ng $g_{w.w.}^{-1}$ for 1 days). Abbreviations: k_{uf}, uptake rate *via* food (expressed d^{-1}); k_{ee}, elimination rate *via* excretion (expressed d^{-1}); biomagnification factor (BMF); BMF$_k$, kinetic BMF; BMF$_{ss}$, BMF steady-state BMF.

Exposure-regime effects. Significant differences in uptake and depuration were observed between the two exposure concentrations/methods for all parameters, including the elimination rates. BMF values were consistently higher under the short-term low-dose regime for both particle sizes. Specifically, BMF$_{ss}$ values were 239 ± 64 for 20 nm nPS and 275 ± 43 for 250 nm nPS during the five-day low-dose exposure, compared to 9 ± 0.9 and 10 ± 1.1, respectively, under the single-day high-dose exposure. Similarly, BMF$_k$ values were markedly higher under the low-dose regime (334 ± 30 for 20 nm and 694 ± 45 for 250 nm) than under the high-dose regime (31 ± 2.0 and 13 ± 0.7, respectively). These results emphasize that biomagnification potential is greater under environmentally relevant low-dose conditions, likely due to prolonged exposure and sustained uptake, despite lower absolute concentrations. This finding highlights the importance of considering chronic dietary exposure scenarios when assessing NP bioaccumulation and ecological risk.

Uptake (k_{uf}). Under the low-dose regime, k_{uf} differed by size (172.5 ± 12.5 d^{-1} for 20 nm; 84.3 ± 10 d^{-1} for 250 nm; $p < 0.005$). In the single-day high-dose regime, k_{uf} values were similar between sizes (10.5 ± 0.6 d^{-1} and 10.0 ± 0.8 d^{-1}), as expected for a single feeding event.

Elimination (k_{ee}). With low-dose exposure, k_{ee} values were 0.25 ± 0.04 (20 nm) and 0.25 ± 0.02 d^{-1} (250 nm), giving biological half-lives ($t_{0.5}$) of 2.7 ± 0.4 d and 2.8 ± 0.03 d, respectively. Under high-dose exposure, k_{ee} values differed by size (0.33 ± 0.02 d^{-1} for 20 nm; 0.75 ± 0.07 d^{-1} for 250 nm; $p < 0.005$), corresponding to $t_{0.5}$ of 2.1 ± 0.2 d and 0.9 ± 0.09 d. These results suggest size-dependent elimination in the single-day dosing context. Consistent with first-order depuration, concentrations declined exponentially following uptake.

Spatially-resolved analysis: organ-specific patterns

QWBA robustness. The robustness of the QWBA was confirmed by: (i) comparing phosphor screen and real-time autoradiography, (ii) quantifying background contributions, and (iii) performing Monte Carlo simulations for organ-specific detector efficiency. All methods produced consistent LOD and LOQ values (Table S2, Fig. S3). Background ^{14}C contributed <1.75% of detected activity, confirming that measurements reflect [^{14}C]nPS (Text S2). Monte Carlo simulations indicated negligible organ-specific bias, except for the skeleton (Table S5). These results confirm QWBA as a reproducible and robust technique for spatially-resolved toxicokinetics.

Single-day high-dose exposure (one feed at 250 ng $g_{w.w.}^{-1}$). Fig. 3 presents the temporal distribution of [^{14}C]nPS_{20} in whole-body autoradiograms at 0.2, 1, and 4 days.

[^{14}C]nPS_{20}. At 0.2 days post-exposure (Fig. 3a), [^{14}C]nPS_{20} activity was localised primarily in the oesophagus, stomach, pyloric caeca, intestine, kidney, fins, eyes, and teeth, indicating the immediate ingestion of labelled particles and quick movement towards the bloodstream.

By 1 day (Fig. 3b), activity was concentrated in the pyloric caeca, intestine and kidney, demonstrating the progressive passage of particles through the digestive system. Quantitative analysis (Fig. 3d) showed the highest [^{14}C]nPS_{20} concentration in the kidney (294.6 $\mu g_C\ g_{w.w.}^{-1}$), suggesting early renal accumulation or filtration. [^{14}C]nPS_{20} was also detected in the liver, with concentrations of 5.4 $\mu g_C\ g_{w.w.}^{-1}$ at 1 day and 61.7 $\mu g_C\ g_{w.w.}^{-1}$ at 4 days, and in the pyloric caeca, where concentrations remained relatively high (125.5–253.5 $\mu g_C\ g_{w.w.}^{-1}$) before decreasing to 28.2 $\mu g_C\ g_{w.w.}^{-1}$ by day 4.

At 4 days post-exposure (Fig. 3c), autoradiograms revealed faint but distinct activity near the hepatic and renal regions, as well as in other organs including the eyes, bones, fins, and skin, suggesting particle redistribution from the gastrointestinal tract over time. The measured activities were above the LOD but close to the LOQ (2.89×10^{-3} $\mu g\ g_{w.w.}^{-1}$), indicating that a limited degree of systemic translocation occurred, although the signal intensity prevents precise quantification. The delayed activity observed in the kidney and liver supports the hypothesis that small [^{14}C]nPS_{20} particles can transiently cross biological barriers.

[^{14}C]nPS_{250}. Activity was below LOQ in most organs, with detectable levels confined to the digestive tract and intestine (Fig. S6, Table S2). These findings provide spatially resolved evidence for size-dependent distribution, with broader organ presence for 20 nm than 250 nm particles.

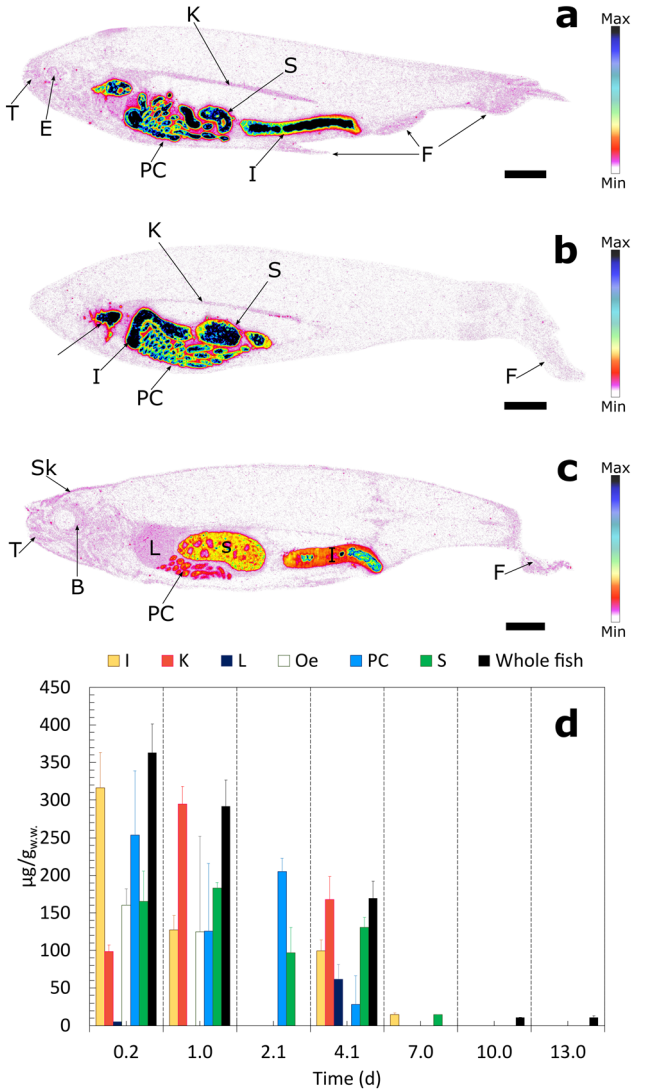

Fig. 3 Quantitative whole-body autoradiography analysis of [^{14}C]nPS_{20} in *O. mykiss* following single-day high-dose exposure to 250 ng $g_{w.w.}^{-1}$ at (a) 0.2 day, (b) 1 day, and (c) 4 days post-ingestion. Colour scales represent linear signal-to-noise (S/N) ratios; scale bars = 1 cm. Corresponding histological sections are provided in Fig. S7. (d) Organ-specific [^{14}C]nPS_{20} quantification (µg $g_{w.w.}^{-1}$) above the LOD (9.53×10^{-4} µg $g_{w.w.}^{-1}$) and LOQ (2.89×10^{-3} µg $g_{w.w.}^{-1}$). Panels (a–d) show [^{14}C]nPS_{20} only; [^{14}C]nPS_{250} signals were GI-confined and below LOQ in systemic tissues at these time points (see Fig. S6, Table S2). Error bars represent inter-section variability (n = 12). Abbreviations: B (bone), E (eye), F (fin), Gi (gills), I (intestine), K (kidney), L (liver), M (muscle), Oe (oesophagus), PC (pyloric caeca), Sk (skin), S (stomach), T (teeth).

Environmentally relevant low-dose exposure (5d at 8 ng $g_{w.w.}^{-1}$). Fig. 4 summarises spatial and temporal patterns across major organs during exposure and depuration.

Tissue distribution. In fish exposed to [^{14}C]nPS_{20} (Fig. 4a), radioactivity was detected in the stomach, pyloric caeca, and intestine, with evidence of translocation *via* the circulatory system into deeper organs such as the liver, kidney, eyes, and bones. A similar, though less pronounced, pattern was

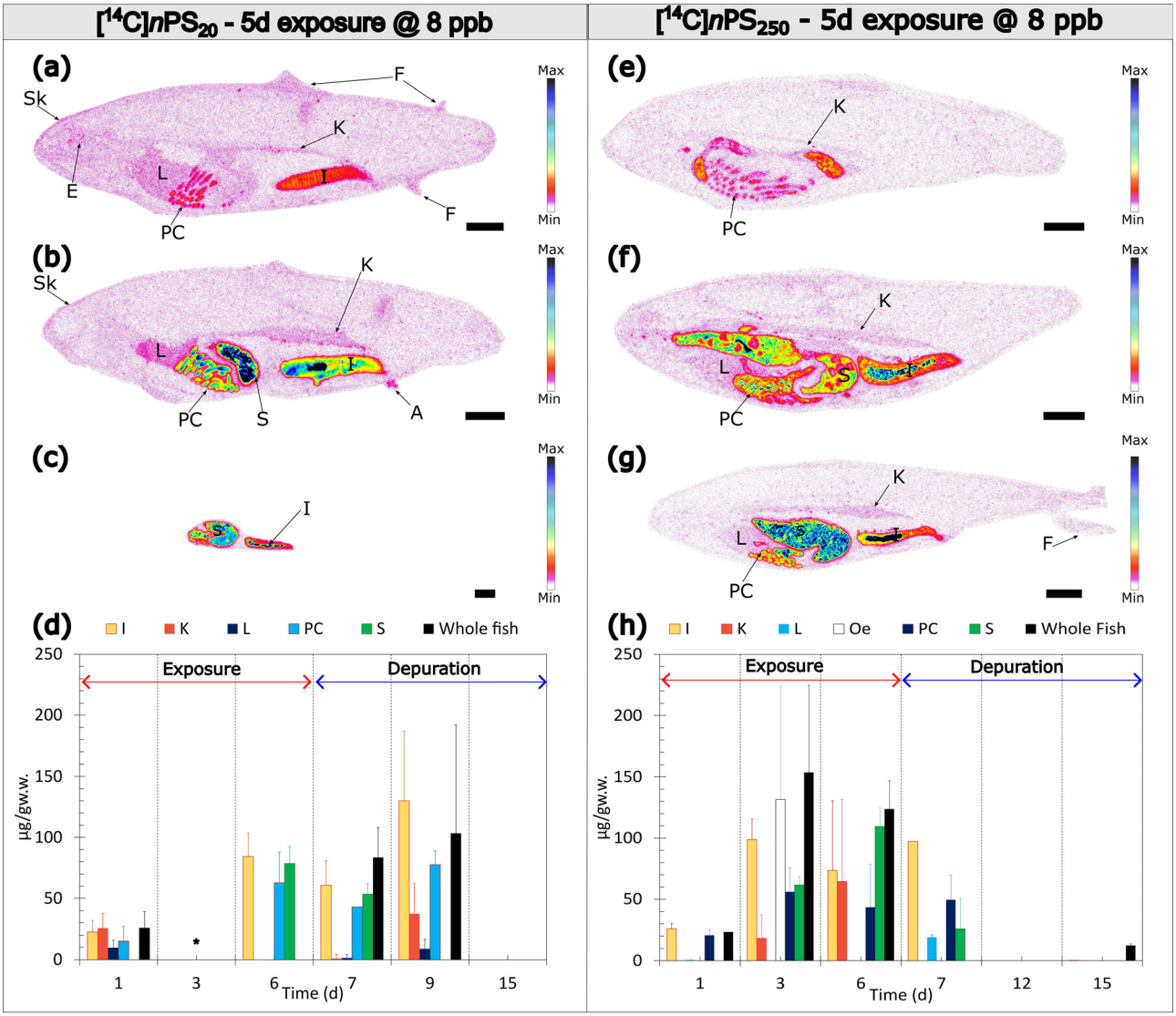

Fig. 4 Quantitative whole-body autoradiography (QWBA) images of the distribution of [^{14}C]nPS in *O. mykiss* after 5 days of dietary exposure followed by 7 day depuration phase. Autoradiograms show distribution of 20 nm (a–c) and 250 nm (e–g) particles at (a and e) 0.2 day, (b and f) 1 day, and (c and g) 4 days ingestion. Organ-specific ^{14}C quantification through time is presented in (d) and (h), where 0 d represents the start of exposure. Colour intensities correspond to the signal-to-noise (S/N) ratio (linear scale; higher intensity = higher [^{14}C]nPS concentration). The scale bar represents 1 cm. Physical tissue sections associated with the autoradiograms are provided in Fig. S8 and S9. Data in (d) and (h) (mean ± SD, *n* = 12) are above the LOD (3.31×10^{-3} µg $g_{w.w.}^{-1}$) and LOQ (1.01×10^{-2} µg $g_{w.w.}^{-1}$). Abbreviations: B (bone), E (eye), Fi (fin), Gi (gills), I (intestine), K (kidney), L (liver), M (muscle), PC (pyrolic ceca), Sk (skin), and S (stomach). *The absence of a visible signal for 20 nm particles at day 3 reflects concentrations below the autoradiography quantification threshold rather than absence of particles.

observed for [^{14}C]nPS$_{250}$ (Fig. 4b), where signal intensity was strongest in the gastrointestinal tract and lower in the skin and liver. This behaviour contrasts with the limited tissue distribution observed under single-day high-dose (24 h) high-dose exposure (Fig. S6).

Organ kinetics. Toxicokinetic assessment of each organ was feasible for both [^{14}C]nPS$_{20}$ and [^{14}C]nPS$_{250}$ (Fig. 4d and h). Distinct organ kinetics were observed between the two particle sizes. The concentration of [^{14}C]nPS$_{20}$ remained relatively constant throughout the 5-day exposure and up to 3 days post-exposure (*i.e.*, 9 days in all), followed by a sharp decline by day 15 when no organs were above detection limits. The highest concentrations of [^{14}C]nPS$_{250}$ occurred after 3 d of exposure (153.6 ± 71.4 in the whole fish and 98.9 ± 16.7 μg_C $g_{w.w.}^{-1}$ in the intestine), followed by a general decrease, except in the stomach and kidney where concentrations continued to increase up to 6 days (109.6 ± 15.1 and 64.7 ± 66.9 μg_C $g_{w.w.}^{-1}$, respectively).

Discussion

Integrated summary of size-dependent uptake and clearance

Our combined TK and QWBA data demonstrate a clear size dependence in the dietary uptake and fate of intrinsically

^{14}C-labelled nPS in juvenile rainbow trout. Following ingestion, both sizes (20 and 250 nm) exhibit early localisation within the gastrointestinal (GI) tract, but only the 20 nm fraction shows short-lived, low-level signals beyond the GI tract—most consistently in hepatic and renal regions—before elimination. In contrast, 250 nm particles remain GI-confined across the time course. TK time series in whole-body tissues and faeces (Fig. 1a–d) reveal rapid, first-order depuration for both sizes once feeding ceases, with tissue burdens returning close to background within ~10 days under the regimes tested. Together, these findings support transient systemic access for 20 nm particles at environmentally relevant doses and minimal parenchymal retention for either size. Fig. 5 provides a conceptual overview of routes and compartments pertinent to dietary uptake and potential enterohepatic recirculation.

In this conceptual view, dietary ingestion would first load the stomach and pyloric caeca; sub-100–200 nm particles then cross local epithelia (gut-associated lymphoid tissue: GALT) and enter either the portal venous circulation to the liver or the lymphatic route to systemic blood.[23,24,31,35] In the liver, opsonisation and Kupffer cell uptake drive rapid handling, with a proportion returning to the intestinal lumen *via* bile (enterohepatic recirculation), consistent with the faecal peaks observed in Fig. 1b and d. Larger particles (≈250 nm) are predominantly retained luminally and cleared as faeces because their size exceeds efficient endocytosis thresholds.[23,31] Once in blood, particles may associate with circulating cells, facilitating short-range transport; systemically, splenic filtration (~150 nm) and renal size selectivity (<10 nm filtration; mesangial/peritubular interactions for larger) constrain residence and promote clearance.[36–41] Transient ocular/skeletal signals should be interpreted cautiously in light of the skeleton detector-efficiency caveat (Table S5). The arrow weights in Fig. 5 reflect the size-dependence seen in QWBA: robust GI → liver → lumen loops for 20 nm, weak/absent systemic arrows for 250 nm (Fig. 3 and 4).

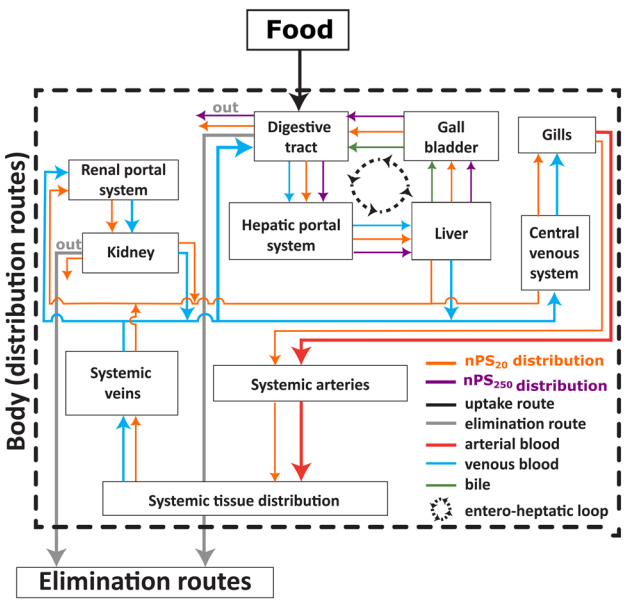

Fig. 5 Conceptual model of nPS_{20} and nPS_{250} distribution mechanisms in rainbow trout (*O. mykiss*), highlighting absorption sites in the stomach and liver during dietary exposure (adapted from Al-Sid-Cheikh *et al.*, 2019).

Why tissue concentrations can exceed faecal concentrations during exposure

Although spiked feed was consumed within minutes, apparent tissue concentrations can temporarily exceed faecal loads during the exposure phase. This arises from two concurrent processes: (i) epithelial absorption of a fraction of ingested particles across the gut wall, followed by a brief presence in vascularised tissues (*e.g.* liver, kidney) until clearance; and (ii) luminal egestion of the non-absorbed fraction over hours to days. Once particles enter circulation—even briefly—they contribute to measurable tissue burdens, whereas faecal concentrations primarily reflect the non-absorbed fraction. This mechanistic dichotomy—absorption with transient retention *vs.* luminal egestion—explains the early maxima and the 1–2 day lag to faecal peaks (Fig. 1b and d). Fig. 5 highlights the gut as the primary absorption site and the liver as a secondary processing compartment.[35]

Mechanistic interpretation of epithelial transport and transient systemic access

The spatial patterns resolved by QWBA (Fig. 3 and 4) are consistent with known size constraints on epithelial transport. Nanoparticles in the sub-100–200 nm range can traverse mucosal barriers through endocytic pathways (*e.g.*, clathrin/caveolae-mediated endocytosis, macropinocytosis) and thereby reach portal venous or lymphatic routes. Particles of ~250 nm are more likely retained luminally and eliminated in faeces.

In fish, gut-associated lymphoid tissue (GALT)—a network of immune structures embedded within the intestinal mucosa—plays a central role in antigen sampling and immune surveillance and offers plausible sampling of particulate matter directly from the lumen. GALT contains lymphoid aggregates and specialized epithelial cells capable of internalizing particulate matter from the gut lumen. Sub-100–200 nm particles can cross intestinal epithelia *via* transcellular endocytic pathways (*e.g.*, clathrin-mediated endocytosis, macropinocytosis), enabling access to GALT and, transiently, systemic circulation.[23,24,31,35]

Once internalised, particle surfaces will acquire a protein corona that promotes opsonisation and recognition by the mononuclear phagocyte system (MPS)—notably Kupffer cells in the liver and macrophages in the spleen—facilitating fast handling and redistribution.[42] This fast handling is well documented for uncoated engineered gold nanoparticles (ENP-Au).[36,43,44] We note that the reported size thresholds for splenic slits (around 100 nm)[37] and renal filtration (effective

mainly for particles <10 nm)[38] come from mammalian studies. Since fish differ anatomically and physiologically, these values cannot be directly transferred, and the thresholds for *O. mykiss* should be viewed as approximate. Within this framework, the renal signal observed for 20 nm particles is most reasonably interpreted as non-glomerular handling (*e.g.*, mesangial/peritubular associations, vascular trapping, immune sequestration) rather than efficient filtration.

The 20 nm kidney signal most plausibly reflects non-glomerular handling (*e.g.*, peritubular uptake, vascular trapping, immune sequestration) rather than filtration. For context, mammalian nanoparticle literature typically places efficient renal filtration in the very small domain (≤~10 nm). Accordingly, our data do not allow estimation of a fish glomerular size cut-off.

Influence of the dosing regime on apparent accumulation

The two dietary regimes—single-day high-dose and five-day low-dose—map complementary regions of the exposure–response space. The single-day high-dose design, while mechanistically useful to accentuate size differences, can over-represent short-lived systemic signals relative to chronic environmental exposure. The five-day low-dose design better mimics chronic dietary intake: under sustained feeding, apparent accumulation metrics (*e.g.*, BMF) rise during the uptake phase even as elimination proceeds; once exposure stops, rapid depuration collapses these metrics. The qualitative differences evident in Fig. 1 (tissues and faeces) and Fig. 4 (organ traces) highlight that regime choice (dose, duration, feeding schedule) strongly shapes apparent bioaccumulation without implying long retention.

Interpreting particulate bioaccumulation metrics (k_{uf}, k_{ee}; BMF_k, BMF_{ss})

TK fitting (*MOSAIC*) provides exposure-regime-dependent uptake *via* food (k_{uf}) and elimination *via* excretion (k_{ee}), along with bioaccumulation metrics (BMF_k and BMF_{ss}). Two considerations are central for particulates:

1) BMF > 1 during multi-day exposure reflects sustained dietary input and short-lived internalisation, not the long biological half-lives characteristic of hydrophobic organic chemicals. Under the five-day low-dose regime, BMF values are higher than under single-day dosing because prolonged feeding raises the numerator (predator burden during uptake), while elimination continues; after exposure ceases, first-order depuration reduces BMF rapidly.

2) Size and regime dependence in k_{uf} and k_{ee} track the threshold-like nature of epithelial transport and immune/biliary handling. In the low-dose context, 20 nm particles typically exhibit a higher k_{uf} than 250 nm, consistent with more effective barrier crossing, whereas elimination constants may be similar or slightly slower for 20 nm due to brief residence in hepatic or reticulo-endothelial compartments prior to clearance. In single-day dosing, the 250 nm fraction can show a faster apparent k_{ee} consistent with dominant luminal egestion and minimal systemic access.

Practically, BMF_k/BMF_{ss} should not be read as evidence for trophic magnification in the classical sense for NPs; rather, they quantify exposure-phase internalisation under the tested diet regimes.

QWBA robustness

We established QWBA's robustness through cross-platform comparison (phosphor screens *vs.* real-time autoradiography), internal embedded standards, and Monte Carlo simulations for detector efficiency across tissues (see SI: Text S2, Fig. S2 and S3, Table S5). Background ^{14}C contributions were minimal, and limits of detection/quantification were consistent between platforms. One caveat is a modest efficiency bias in skeletal regions; because dense mineralised matrices can modestly alter β detection efficiency, skeletal signals were interpreted conservatively. Bone detection were reproducible across sections/animals, anatomically plausible, and—where available—confirmed across platforms. Skeletal signals are reported qualitatively. These checks support confidence in spatial trends while acknowledging known analytical constraints.

Post-epithelial handling: MPS, biliary clearance, immune-mediated redistribution

Once across the epithelium, protein-corona formation and opsonisation favour Kupffer cell uptake in the liver and sequestration by splenic macrophages; together these processes constitute rapid MPS handling. Biliary excretion provides a route back to the intestinal lumen (enterohepatic cycling), consistent with faecal peaks following or overlapping tissue maxima (Fig. 1b and d). The immune system (macrophages, neutrophils) can drive redistribution and local inflammatory signalling, potentially contributing to organ-to-organ movement at low levels.[45–47] This is captured by QWBA as faint extra-GI signals for 20 nm early in depuration. The absence of persistent muscle burdens and the short whole-body half-lives argue against meaningful long-term storage under the conditions studied.

Organ-specific kinetics and spatial–temporal patterns

QWBA images and quantification (Fig. 3 and 4; SI Fig. S6–S9) allow time-resolved insight into organ kinetics. For 20 nm particles under high-dose single-feeding, signals localise rapidly to the stomach, pyloric caeca, intestine, with transient presence in kidney and hepatic regions at early time points (Fig. 3a–d). Under five-day low-dose exposure, GI compartments (stomach, pyloric caeca, intestine) dominate, with lower-intensity but detectable signals in liver, kidney, skin, fins, and eyes (Fig. 4a–d). For 250 nm, signals remain GI-confined and below LOQ in systemic organs at matched time points (Fig. 4e–h; Fig. S6). These patterns align with the

size-limited transport and rapid clearance mechanisms described above.

Dissolved-chemical paradigm mispredicts NP behaviour

The uptake and depuration kinetics of nPS observed in this study differ fundamentally from those of metals and persistent organic pollutants (POPs). Metals such as methylmercury and cadmium exhibit biological half-lives of weeks to months due to strong binding to proteins and slow elimination,[48] whereas POPs (*e.g.*, PCBs, DDT) persist for months to years in fish tissues, driven by high lipophilicity ($\log K_{ow} > 6$) and limited biotransformation;[49,50] these properties result in high biomagnification potential (BMF commonly 5–20, occasionally > 100 in top predators).[49–51] In contrast, nPS particles behave as discrete particulates: translocation and clearance are size-dependent, with near-complete depuration under the exposure regimes tested (see Fig. 1; Table S4). NP behaviour therefore does not follow classical bioaccumulation paradigms based on solubility and lipophilicity but is governed by particle size, morphology, and surface properties.[5] Comparable size-dependent biodistribution has been reported for ENP-Au and ENP-Ag, including preferential accumulation in liver and spleen.[39,52–54] Consequently, risk assessment frameworks designed for dissolved chemicals may not adequately capture the behaviour of NPs characterised by short-lived internalisation and limited potential for long-term retention under environmentally relevant conditions.

Environmental realism, exposure design, and limitations

We examined sub-100 nm particles (nanomaterial-like behaviour) alongside 250 nm particles (upper nanoscale), to bracket thresholds for uptake and clearance in relation to definitions of NPs (<1000 nm).[6] The single-day high-dose scenario is informative mechanistically (clear size contrast, convenient kinetics) but can over-represent transient systemic signals relative to chronic environmental exposure; conversely, the five-day low-dose regime better mimics chronic dietary intake and yielded distinct dynamics (higher BMF during exposure, similar rapid clearance post-exposure). Together, these regimes map the exposure–response space and emphasise that regime choice (dose and duration) strongly shapes apparent accumulation metrics—even when long-term retention is limited. Several caveats warrant emphasis:

- **Particle identity**: we used pristine, spherical polystyrene as a benchmark to isolate particle size effects at controlled dose, supported by intrinsic ^{14}C labelling and QWBA for sensitive, spatially resolved quantification.[5,17,20] Environmental particles, however, are typically aged/heterogeneous: oxidation introduces oxygen-containing groups (*e.g.*, hydroxyl, carbonyl, carboxyl),[55–57] roughness increases, and surfaces host biofilms;[58] these changes alter hydrophilicity, charge and aggregation, and can enhance contaminant sorption,[58–60] thereby modulating membrane interactions, kinetics and toxicity.[61] Future work should therefore incorporate aged/weathered polymers and chronic low-level dietary regimes to resolve how surface chemistry, roughness, sorbed contaminants and biofilms impact translocation, tissue distribution and trophic transfer.
- **Species physiology**: Species-specific physiology (*e.g.*, spleen architecture, renal thresholds) may shift size gates relative to mammalian benchmarks; we therefore avoid hard cut-offs for fish and treat extra-mammalian inferences cautiously.

Despite these limitations, the integrated TK–QWBA approach quantitatively resolves size-dependent biodistribution and clearance at realistic concentrations, providing a contamination-resistant alternative to dissection-based quantification and a strong basis for mechanistic inference.

Ecological and trophic transfer implications

From a consumer perspective, rapid depuration and negligible muscle retention argue for limited long-term body burdens, reducing direct human exposure *via* fillets under conditions comparable to this study. Ecologically, however, transient internalisation during the diet phase implies the possibility of trophic transfer, especially under chronic, low-level exposures or in species with slower gut transit and different immune handling. Beyond mass balance, functional endpoints (digestion efficiency, mucus production, immune tone, epithelial integrity) deserve attention because the short-lived presence can still modulate physiology in ways not captured by bulk concentration metrics alone.

Policy and assessment implications

The data advocate a shift from dissolved-chemical paradigms toward particle-kinetic modelling for NPs. Practically, this means:

(i) prioritising chronic, low-dose dietary studies to quantify exposure-phase internalisation without conflating it with long retention;

(ii) incorporating aged/weathered particles (oxidised, roughened, biofilm-bearing; with sorbed co-contaminants) to capture environmental realism; and

(iii) embedding fish-specific physiology (*e.g.*, spleen/renal size selectivity) in bioaccumulation models to avoid mammal-centric biases. These steps will improve ecological realism and regulatory relevance.

Conclusions

Intrinsic ^{14}C labelling combined with QWBA provides a sensitive, contamination-resistant route to quantify and image NP biodistribution at environmentally relevant concentrations. By embedding ^{14}C in the polymer backbone, we achieve accurate spatial quantification without dissection.

Our data reveal size-dependent toxicokinetics: 20 nm nPS transiently appears in hepatic/renal regions while 250

nm remains GI-confined; both sizes depurate rapidly ($t_{1/2}$ ≈ 0.9–2.7 d; near-complete clearance ≤ ~10 d). Exposure regime matters: multi-day low-dose feeding elevates apparent accumulation during uptake relative to single-day dosing, yet post-exposure depuration is rapid. *MOSAIC* modelling confirms this with k_{uf}/k_{ee} estimates and BMF metrics, where higher BMF_k/BMF_{ss} under low-dose reflects sustained dietary input, not long retention.

Spatially resolved QWBA shows organ-specific patterns (pyloric caeca, intestine, liver) for 20 nm consistent with GALT-mediated transport and endocytic pathways. A modest detector-efficiency bias in skeletal regions was noted; accordingly, bone signals were interpreted conservatively.

Collectively, NPs in fish behave as particulates, not as dissolved lipophilic chemicals: size, morphology and surface chemistry govern brief internalisation and rapid elimination. These insights argue for particle-kinetic models and chronic, realistic dietary studies—including aged/biofilm-bearing particles—to refine ecological risk, trophic-transfer assessments and policy guidance.

Author contributions

The manuscript was written through contributions of all authors. All authors have given approval to the final version of the manuscript. Conceptualization, MASC, JWLA, GTL, AIC, TBH, SJR, MAC, RCT; data curation MASC, JWLA, GTL; formal analysis, MASC, JWLA; funding acquisition TBH, SJR, RCT; investigation, MASC, JWLA, GTL, AIC, TBH, SJR, MAC, RCT; methodology, MASC, JWLA, GTL; project administration, TBH, SJR, RCT; resources, TBH, SJR, RCT; software, MASC, JWLA; supervision TBH, SJR, RCT; validation, MASC, JWLA, GTL; visualization, MASC, JWLA; roles/writing – original draft, MASC; and writing – review & editing, MASC, JWLA, GTWL, AIC, TBH, SJR, MAC, RCT.

Conflicts of interest

There are no conflicts to declare.

Abbreviations

[^{14}C]nPS	^{14}C-labelled nanopolystyrene particles
ATR	Attenuated total reflection
BMF	Biomagnification factors
BMF_k	Biomagnification factors given as probability distributions: kinetic
BMF_{ss}	BMF at steady-state
CMC	Carboxymethylcellulose
DLU	Digital light units
Dpm	Disintegration per minutes
ENPs	Engineered nanoparticles
F_E	Fraction of electrons emitted
FLA	Fluorescent image analyzer
FTIR	Fourier-transform infrared spectroscopy
k_{ee}	Elimination rates of excretion
KPS	Potassium persulfate
k_{uf}	Uptake rate of food
LOD	Limit of detection
LOQ	Limit of quantification
MDA	Minimum detectable activity
$MOSAIC_{bioacc}$	MOdeling and StAtistical tools for ecotoxicology
NaOH	Sodium hydroxide
NPs	Nanoplastics
nPS	nanopolystyrene
pH	potential hydrogen
PMMA	Poly(methyl methacrylate)
PSL	Photostimulated luminescence
Toxicokinetics	TK
QWBA	Quantitative-whole body autoradiography
S.D.	Standard deviation
SDS	Sodium dodecyl sulfate

Data availability

The data that support the findings of this study are available from the corresponding author upon reasonable request.

Supplementary information (SI): includes details on the radiosynthesis and characterisation of [^{14}C]nPS (Text S1), calibration and validation of the quantitative whole-body autoradiography method (Text S2), and toxicokinetic modelling (Text S3). Additional data are provided in the form of FTIR and Raman spectroscopy analyses of particles (Fig. S1), calibration curves for QWBA (Fig. S2), comparison of autoradiographs from BeaQuant and phosphor screen autoradiography (Fig. S3), and MOSAIC Bioacc modelling for tissue and faeces analyses (Fig. S4 and S5). Autoradiography images and corresponding physical tissue section photographs from rainbow trout exposed to [^{14}C]nPS under single-day high-dose and chronic conditions are presented in Fig. S6–S9. Experimental design and sampling timelines, limits of detection and quantification for the analytical techniques used, elemental composition of Monte Carlo simulated organs, MOSAIC Bioacc parameter estimates, and emission fractions of ^{14}C from different organs are provided in Tables S1–S5. See DOI: https://doi.org/10.1039/d5en00985e

Acknowledgements

We thank the Heriot Watt University technical staff and Radioprotection supervisor A. Bolton for support throughout the exposure experiment. We thank the University of Plymouth Consolidated Radio-isotope Facility (W. Blake, A. Taylor, G. Millward and N. Crocker) for support for the radioactivity work. This research was part of the RealRiskNano project funded by the Natural Environment Research Council, UK (grant number: NE/N006526/1) to whom we are grateful. All analysis and data were only possible with the Applied RadioIsotope laboratory (grant number: NE/V017616/1), the mobility fellowship from the Royal society (grant number: RM1802-0440), and The CAMS

funding (grant number: 600310/10) to whom we are grateful. This research was supported by the scholarship funding from the National Research Foundation, Singapore, and a grant from the Jenny and Antti Wihuri Foundation (grant number: 00220019). We would also like to thank Prof Émilien Pelletier (*emeritus*) and Ariane Plourde (Director, ISMER-UQAR) for providing access to the CM3600 Leica. This work has received approval for research ethics from Home Office and a proof of approval is available upon request.

Notes and references

1 J. Gigault, A. Halle, M. Baudrimont, P.-Y. Pascal, F. Gauffre, T.-L. Phi, H. El Hadri, B. Grassl and S. Reynaud, Current Opinion: What Is a Nanoplastic?, *Environ. Pollut.*, 2018, **235**, 1030–1034, DOI: 10.1016/j.envpol.2018.01.024.

2 J. Alexander, L. Barregård, M. Bignami, S. Ceccatelli, B. Cottrill, M. Dinovi, L. Edler, B. Grasl-Kraupp, C. Hogstrand, L. (Ron) Hoogenboom, H. K. Knutsen, C. S. Nebbia, I. Oswald, A. Petersen, V. M. Rogiers, M. Rose, A.-C. Roudot, T. Schwerdtle, C. Vleminckx, G. Vollmer and H. Wallace, EFSA Panel on Contaminants in the Food Chain (CONTAM). Presence of microplastics and nanoplastics in food, with particular focus on seafood, *EFSA J.*, 2016, **14**(6), DOI: 10.2903/j.efsa.2016.4501.

3 N. B. Hartmann, T. Hüffer, R. C. Thompson, M. Hassellöv, A. Verschoor, A. E. Daugaard, S. Rist, T. Karlsson, N. Brennholt, M. Cole, M. P. Herrling, M. C. Hess, N. P. Ivleva, A. L. Lusher and M. Wagner, Are We Speaking the Same Language? Recommendations for a Definition and Categorization Framework for Plastic Debris, *Environ. Sci. Technol.*, 2019, **53**(3), 1039–1047, DOI: 10.1021/acs.est.8b05297.

4 J. P. G. L. Frias and R. Nash, Microplastics: Finding a Consensus on the Definition, *Mar. Pollut. Bull.*, 2019, **138**, 145–147, DOI: 10.1016/j.marpolbul.2018.11.022.

5 M. Al-Sid-Cheikh, S. J. Rowland, K. Stevenson, C. Rouleau, T. B. Henry and R. C. Thompson, Uptake, Whole-Body Distribution, and Depuration of Nanoplastics by the Scallop Pecten Maximus at Environmentally Realistic Concentrations, *Environ. Sci. Technol.*, 2018, **52**(24), 14480–14486, DOI: 10.1021/acs.est.8b05266.

6 SAPEA, *Scientific Perspective on Microplastics in Nature and Society | SAPEA, Evidence Review Report*, 2019, DOI: 10.26356/microplastics.

7 R. Geyer, J. R. Jambeck and K. L. Law, Production, Use, and Fate of All Plastics Ever Made, *Sci. Adv.*, 2017, **3**(7), e1700782, DOI: 10.1126/sciadv.1700782.

8 L. Lebreton and A. Andrady, Future Scenarios of Global Plastic Waste Generation and Disposal, *Palgrave Commun.*, 2019, **5**(1), 6, DOI: 10.1057/s41599-018-0212-7.

9 I. Tiseo, *Plastic Waste Worldwide - Statistics & Facts*, 2023, https://www.statista.com/topics/5401/global-plastic-waste/#topicOverview (accessed 2023-07-17).

10 UNEP, C. Llorenç Milà i, C. Alison, L. Peggy, M. Allan, R. Andrew David, S. Aphrodite, S. Steven, T. Elisa, S. Yoni, F. de la José, K. Julia, T. B. Anne, B. Eline, F. Steve, M. Antaya, R. Keiron and B. Andrea, *Turning off the Tap: How the World Can End Plastic Pollution and Create a Circular Economy*, Geneva, 2023, https://wedocs.unep.org/bitstream/handle/20.500.11822/42277/Plastic_pollution.pdf?sequence=1&isAllowed=y (accessed 2023-07-17).

11 R. Lenz, K. Enders and T. G. Nielsen, Microplastic Exposure Studies Should Be Environmentally Realistic, *Proc. Natl. Acad. Sci. U. S. A.*, 2016, **113**(29), E4121–E4122, DOI: 10.1073/pnas.1606615113.

12 E. M. Cunningham and J. D. Sigwart, Environmentally Accurate Microplastic Levels and Their Absence from Exposure Studies, *Integr. Comp. Biol.*, 2019, **59**(6), 1485–1496, DOI: 10.1093/icb/icz068.

13 D. Materić, H. A. Kjær, P. Vallelonga, J.-L. Tison, T. Röckmann and R. Holzinger, Nanoplastics Measurements in Northern and Southern Polar Ice, *Environ. Res.*, 2022, **208**, 112741, DOI: 10.1016/j.envres.2022.112741.

14 N. J. Clark, F. R. Khan, C. Crowther, D. M. Mitrano and R. C. Thompson, Uptake, Distribution and Elimination of Palladium-Doped Polystyrene Nanoplastics in Rainbow Trout (Oncorhynchus Mykiss) Following Dietary Exposure, *Sci. Total Environ.*, 2023, **854**, 158765, DOI: 10.1016/j.scitotenv.2022.158765.

15 D. M. Mitrano, A. Beltzung, S. Frehland, M. Schmiedgruber, A. Cingolani and F. Schmidt, Synthesis of Metal-Doped Nanoplastics and Their Utility to Investigate Fate and Behaviour in Complex Environmental Systems, *Nat. Nanotechnol.*, 2019, **14**(4), 362–368, DOI: 10.1038/s41565-018-0360-3.

16 M. B. Paul, V. Stock, J. Cara-Carmona, E. Lisicki, S. Shopova, V. Fessard, A. Braeuning, H. Sieg and L. Böhmert, Micro- And Nanoplastics-Current State of Knowledge with the Focus on Oral Uptake and Toxicity, *Nanoscale Adv.*, 2020, 4350–4367, DOI: 10.1039/d0na00539h.

17 M. Al-Sid-Cheikh, S. J. Rowland, R. Kaegi, T. B. Henry, M.-A. Cormier and R. C. C. Thompson, Synthesis of 14C-Labelled Polystyrene Nanoplastics for Environmental Studies, *Commun. Mater.*, 2020, **1**(1), 97, DOI: 10.1038/s43246-020-00097-9.

18 E. G. Solon, S. K. Balani and F. W. Lee, Whole-Body Autoradiography In Drug Discovery, *Curr. Drug Metab.*, 2002, **3**(5), 451–462, DOI: 10.2174/1389200023337207.

19 E. G. Solon, Use of Radioactive Compounds and Autoradiography to Determine Drug Tissue Distribution, *Chem. Res. Toxicol.*, 2012, **25**(3), 543–555, DOI: 10.1021/tx200509f.

20 E. G. Solon, Autoradiography Techniques and Quantification of Drug Distribution, *Cell Tissue Res.*, 2015, **360**(1), 87–107, DOI: 10.1007/s00441-014-2093-4.

21 E. G. Solon, A. Schweitzer, M. Stoeckli and B. Prideaux, Autoradiography, MALDI-MS, and SIMS-MS Imaging in Pharmaceutical Discovery and Development, *AAPS J.*, 2010, **12**(1), 11–26, DOI: 10.1208/s12248-009-9158-4.

22 M. Al-Sid-Cheikh, C. Rouleau and E. Pelletier, Tissue Distribution and Kinetics of Dissolved and Nanoparticulate Silver in Iceland Scallop (Chlamys

Islandica), *Mar. Environ. Res.*, 2013, **86**, 21–28, DOI: 10.1016/j.marenvres.2013.02.003.

23 S. Barua and S. Mitragotri, Challenges Associated with Penetration of Nanoparticles across Cell and Tissue Barriers: A Review of Current Status and Future Prospects, *Nano Today*, 2014, **9**(2), 223–243, DOI: 10.1016/j.nantod.2014.04.008.

24 A. P. Walczak, E. Kramer, P. J. M. Hendriksen, P. Tromp, J. P. F. G. Helsper, M. van der Zande, I. M. C. M. Rietjens and H. Bouwmeester, Translocation of Differently Sized and Charged Polystyrene Nanoparticles in in Vitro Intestinal Cell Models of Increasing Complexity, *Nanotoxicology*, 2015, **9**(4), 453–461, DOI: 10.3109/17435390.2014.944599.

25 K. Ziani, C.-B. Ioniță-Mîndrican, M. Mititelu, S. M. Neacșu, C. Negrei, E. Moroşan, D. Drăgănescu and O.-T. Preda, Microplastics: A Real Global Threat for Environment and Food Safety: A State of the Art Review, *Nutrients*, 2023, **15**(3), 617, DOI: 10.3390/nu15030617.

26 G. Oberdörster, E. Oberdörster and J. Oberdörster, Nanotoxicology: An Emerging Discipline Evolving from Studies of Ultrafine Particles, *Environ. Health Perspect.*, 2005, **113**(7), 823–839, DOI: 10.1289/ehp.7339.

27 W. G. Kreyling, M. Semmler-Behnke and W. Möller, Ultrafine Particle–Lung Interactions: Does Size Matter?, *J. Aerosol Med.*, 2006, **19**(1), 74–83, DOI: 10.1089/jam.2006.19.74.

28 W. G. Kreyling, M. Semmler, F. Erbe, P. Mayer, S. Takenaka, H. Schulz, G. Oberdörster and A. Ziesenis, Translocation of ultrafine insoluble iridium particles from lung epithelium to extrapulmonary organs is size dependent but very low, *J. Toxicol. Environ. Health, Part A*, 2002, **65**(20), 1513–1530, DOI: 10.1080/00984100290071649.

29 M. Semmler-Behnke, J. Lipka, A. Wenk, S. Hirn, M. Schäffler, F. Tian, G. Schmid, G. Oberdörster and W. G. Kreyling, Size Dependent Translocation and Fetal Accumulation of Gold Nanoparticles from Maternal Blood in the Rat, *Part. Fibre Toxicol.*, 2014, **11**(1), 33, DOI: 10.1186/s12989-014-0033-9.

30 W. H. De Jong, W. I. Hagens, P. Krystek, M. C. Burger, A. J. A. M. Sips and R. E. Geertsma, Particle Size-Dependent Organ Distribution of Gold Nanoparticles after Intravenous Administration, *Biomaterials*, 2008, **29**(12), 1912–1919, DOI: 10.1016/j.biomaterials.2007.12.037.

31 H. Sinnecker, T. Krause, S. Koelling, I. Lautenschläger and A. Frey, The Gut Wall Provides an Effective Barrier against Nanoparticle Uptake, *Beilstein J. Nanotechnol.*, 2014, **5**, 2092–2101, DOI: 10.3762/bjnano.5.218.

32 S. Charles, P. Veber and M. L. Delignette-Muller, MOSAIC: A Web-Interface for Statistical Analyses in Ecotoxicology, *Environ. Sci. Pollut. Res.*, 2018, **25**(12), 11295–11302, DOI: 10.1007/s11356-017-9809-4.

33 A. Ratier and S. Charles, Accumulation-Depuration Data Collection in Support of Toxicokinetic Modelling, *Sci. Data*, 2022, **9**(1), 130, DOI: 10.1038/s41597-022-01248-y.

34 A. Ratier, C. Lopes, G. Multari, V. Mazerolles, P. Carpentier and S. Charles, New Perspectives on the Calculation of Bioaccumulation Metrics for Active Substances in Living Organisms, *Integr. Environ. Assess. Manage.*, 2022, **18**(1), 10–18, DOI: 10.1002/ieam.4439.

35 X. Qiao, L. Bao, G. Liu and X. Cui, Nanomaterial Journey in the Gut: From Intestinal Mucosal Interaction to Systemic Transport, *Nanoscale*, 2024, **16**(41), 19207–19220, DOI: 10.1039/D4NR02480J.

36 C. H. J. Choi, J. E. Zuckerman, P. Webster and M. E. Davis, Targeting Kidney Mesangium by Nanoparticles of Defined Size, *Proc. Natl. Acad. Sci. U. S. A.*, 2011, **108**(16), 6656–6661, DOI: 10.1073/pnas.1103573108.

37 E. C. Dreaden, L. A. Austin, M. A. Mackey and M. A. El-Sayed, Size Matters: Gold Nanoparticles in Targeted Cancer Drug Delivery, *Ther. Delivery*, 2012, **3**(4), 457–478, DOI: 10.4155/tde.12.21.

38 J. E. Zuckerman, C. H. J. Choi, H. Han and M. E. Davis, Polycation-SiRNA Nanoparticles Can Disassemble at the Kidney Glomerular Basement Membrane, *Proc. Natl. Acad. Sci. U. S. A.*, 2012, **109**(8), 3137–3142, DOI: 10.1073/pnas.1200718109.

39 H. Soo Choi, W. Liu, P. Misra, E. Tanaka, J. P. Zimmer, B. Itty Ipe, M. G. Bawendi and J. V. Frangioni, Renal Clearance of Quantum Dots, *Nat. Biotechnol.*, 2007, **25**(10), 1165–1170, DOI: 10.1038/nbt1340.

40 D. W. Bartlett and M. E. Davis, Physicochemical and Biological Characterization of Targeted, Nucleic Acid-Containing Nanoparticles, *Bioconjugate Chem.*, 2007, **18**(2), 456–468, DOI: 10.1021/bc0603539.

41 A. de Barros, A. Tsourkas, B. Saboury, V. Cardoso and A. Alavi, Emerging Role of Radiolabeled Nanoparticles as an Effective Diagnostic Technique, *EJNMMI Res.*, 2012, **2**(1), 39, DOI: 10.1186/2191-219X-2-39.

42 D. OwensIII and N. Peppas, Opsonization, Biodistribution, and Pharmacokinetics of Polymeric Nanoparticles, *Int. J. Pharm.*, 2006, **307**(1), 93–102, DOI: 10.1016/j.ijpharm.2005.10.010.

43 S. A. Kulkarni and S.-S. Feng, Effects of Particle Size and Surface Modification on Cellular Uptake and Biodistribution of Polymeric Nanoparticles for Drug Delivery, *Pharm. Res.*, 2013, **30**(10), 2512–2522, DOI: 10.1007/s11095-012-0958-3.

44 X. Liu, N. Huang, H. Li, Q. Jin and J. Ji, Surface and Size Effects on Cell Interaction of Gold Nanoparticles with Both Phagocytic and Nonphagocytic Cells, *Langmuir*, 2013, **29**(29), 9138–9148, DOI: 10.1021/la401556k.

45 C. Petrarca, E. Clemente, V. Amato, P. Pedata, E. Sabbioni, G. Bernardini, I. Iavicoli, S. Cortese, Q. Niu, T. Otsuki, R. Paganelli and M. Di Gioacchino, Engineered Metal Based Nanoparticles and Innate Immunity, *Clin. Mol. Allergy*, 2015, **13**(1), 13, DOI: 10.1186/s12948-015-0020-1.

46 E. Vivier and B. Malissen, Innate and Adaptive Immunity: Specificities and Signaling Hierarchies Revisited, *Nat. Immunol.*, 2005, **6**(1), 17–21, DOI: 10.1038/ni1153.

47 A.-C. Greven, T. Merk, F. Karagöz, K. Mohr, M. Klapper, B. Jovanović and D. Palić, Polycarbonate and Polystyrene Nanoplastic Particles Act as Stressors to the Innate Immune System of Fathead Minnow (Pimephales Promelas),

Environ. Toxicol. Chem., 2016, **35**(12), 3093–3100, DOI: 10.1002/etc.3501.

48 T. W. Clarkson and L. Magos, The Toxicology of Mercury and Its Chemical Compounds, *Crit. Rev. Toxicol.*, 2006, **36**(8), 609–662, DOI: 10.1080/10408440600845619.

49 F. A. P. C. Gobas, A Model for Predicting the Bioaccumulation of Hydrophobic Organic Chemicals in Aquatic Food-Webs: Application to Lake Ontario, *Ecol. Modell.*, 1993, **69**(1–2), 1–17, DOI: 10.1016/0304-3800(93)90045-T.

50 D. Mackay and A. Fraser, Bioaccumulation of Persistent Organic Chemicals: Mechanisms and Models, *Environ. Pollut.*, 2000, **110**(3), 375–391, DOI: 10.1016/S0269-7491(00)00162-7.

51 B. C. Kelly, M. G. Ikonomou, J. D. Blair, A. E. Morin and F. A. P. C. Gobas, Food Web–Specific Biomagnification of Persistent Organic Pollutants, *Science*, 2007, **317**(5835), 236–239, DOI: 10.1126/science.1138275.

52 M. Al-Sid-Cheikh, C. Rouleau, D. Bussolaro, C. A. Oliveira Ribeiro and E. Pelletier, Tissue Distribution of Radiolabeled 110m Ag Nanoparticles in Fish: Arctic Charr (Salvelinus Alpinus), *Environ. Sci. Technol.*, 2019, **53**(20), 12043–12053, DOI: 10.1021/acs.est.9b04010.

53 S. Hirn, M. Semmler-Behnke, C. Schleh, A. Wenk, J. Lipka, M. Schäffler, S. Takenaka, W. Möller, G. Schmid, U. Simon and W. G. Kreyling, Particle Size-Dependent and Surface Charge-Dependent Biodistribution of Gold Nanoparticles after Intravenous Administration, *Eur. J. Pharm. Biopharm.*, 2011, **77**(3), 407–416, DOI: 10.1016/j.ejpb.2010.12.029.

54 G. Sonavane, K. Tomoda and K. Makino, Biodistribution of Colloidal Gold Nanoparticles after Intravenous Administration: Effect of Particle Size, *Colloids Surf., B*, 2008, **66**(2), 274–280, DOI: 10.1016/j.colsurfb.2008.07.004.

55 D. Feldman, Weathering of Polymers, *J. Polym. Sci., Polym. Lett. Ed.*, 1984, **22**(7), 423, DOI: 10.1002/pol.1984.130220709.

56 D. Feldman, Polymer Weathering: Photo-Oxidation, *J. Polym. Environ.*, 2002, **10**(4), 163–173, DOI: 10.1023/A:1021148205366.

57 B. Gewert, M. M. Plassmann and M. MacLeod, Pathways for Degradation of Plastic Polymers Floating in the Marine Environment, *Environ. Sci.: Processes Impacts*, 2015, **17**(9), 1513–1521, DOI: 10.1039/C5EM00207A.

58 I. Goßmann, H. Mitsutake, J. Degenhardt, M. E. Simonsen and F. Liu, Biofilms on Plastics Slow Photo-Oxidation While Promoting Surface Degradation, *Environ. Sci. Technol.*, 2025, **59**(42), 22866–22873, DOI: 10.1021/acs.est.5c08345.

59 A. Al Harraq, P. J. Brahana, O. Arcemont, D. Zhang, K. T. Valsaraj and B. Bharti, Effects of Weathering on Microplastic Dispersibility and Pollutant Uptake Capacity, *ACS Environ. Au*, 2022, **2**(6), 549–555, DOI: 10.1021/acsenvironau.2c00036.

60 F. Yu, Q. Qin, X. Zhang and J. Ma, Characteristics and Adsorption Behavior of Typical Microplastics in Long-Term Accelerated Weathering Simulation, *Environ. Sci.: Processes Impacts*, 2024, **26**(5), 882–890, DOI: 10.1039/D4EM00062E.

61 S. Oh and E. E. Stache, Recent Advances in Oxidative Degradation of Plastics, *Chem. Soc. Rev.*, 2024, **53**(14), 7309–7327, DOI: 10.1039/D4CS00407H.